Supplementary Information (SI) for Energy & Environmental Science.

Supporting Information

Asymmetric RE-O-Ru unit with bridged oxygen vacancies accelerates deprotonation of acidic water oxidation

Caikang Wang,[+a,b] Xiangrui Wu,[+a] Hao Sun,*[b] Zhe Xu,[a] Chang Xu,[a] Xuan Wang,[a] Meng Li,[a] Yu Wang,[a] Yawen Tang,[a] Jianchun Jiang,[b] Kang Sun,*[b] Gengtao Fu*[a]

[a] Jiangsu Key Laboratory of New Power Batteries, Jiangsu Collaborative Innovation Center of Biomedical Functional Materials, School of Chemistry and Materials Science, Nanjing Normal University, Nanjing 210023, China
*E-mail address: gengtaofu@njnu.edu.cn (G. Fu)

[b] Key Lab. of Biomass Energy and Material, Jiangsu Province, Key and Open Lab. of Forest Chemical Engineering, SFA, National Engineering Lab. for Biomass Chemical Utilization, Institute of Chemical Industry of Forest Products, Chinese Academy of Forestry, Nanjing 210042, China
*E-mail address: sunhao@icifp.cn (H. Sun); sunkang@icifp.cn (K. Sun)

[+] These authors contributed equally to this work.

Reagent and materials

All reagents were analytical reagents with no purified operation. Ru(III) acetylacetonate (Ru(acac)$_3$), Samarium(III) acetylacetonate (Sm(acac)$_3$), Neodymium(III) acetylacetonate (Nd(acac)$_3$), Lutetium(III) acetylacetonate (Lu(acac)$_3$), Potassium bromide (KBr), Ethanol absolute (C_2H_6O) were purchased from Sinopharm Chemical Reagent Co., Ltd. Nafion solution (5 wt%) and Commercial rutile-type RuO_2 (99.9%) were obtained from Sigma-Aldrich. Ultrapure water (18.2 MΩ cm) was used throughout the work.

Synthesis of Sm-RuO_{2-x}-O_v

In a typical synthesis of Sm-doped RuO_2 with bridge oxygen vacancies (denoted as Sm-RuO_{2-x}-O_v, 32 mg Ru(acac)$_2$, 2.0 mg Sm(acac)$_3$ and 300 mg KBr were dissolved into 35 mL mixed solution contenting ethanol and distilled water (the corresponding volume ration is about 6). Under fierce stirring, the solution gradually became clarified dark red. The powder obtained from drying the solution was grinded in agar mortar and subsequently annealed in a tube furnace at 450 °C for 90 min under air atmosphere at a ramp rate of 5 °C min^{-1}. The obtained products were washed thoroughly with DI water and ethanol, finally dried in vacuum chamber (60 °C). The resulting black products were collected. Home-made RuO_2 with bridge oxygen vacancies (denoted as RuO_2-O_v), Sm-RuO_{2-x}-O_v with various Sm contents, other rare earth (RE) doped RuO_2 (*i.e.,* Nd and Lu) were prepared by the same synthetic procedure with different Ru/RE feeding ratios.

Characterization.

The morphology and structure of the as-prepared samples were characterized by the Lorenz Transmission Electron Microscope (TEM, JEOL 2100F) with an acceleration voltage of 200 kV, and corresponding energy dispersive X-ray (EDS) mapping was employed to identify the element composition and distribution. The phase and crystalline structures of the products were characterized by an X-ray diffractometer (XRD, Bruker, AXS) using a Cu Kα radiation source (λ = 1.5406 Å) and manipulated at 40 kV and 100 mA. The surface composition and the valence states of the sample were characterized by X-ray photoelectron spectroscopy (XPS) with Thermo VG Scientific ESCALAB 250 spectrometers with an Al Kα light source. All binding energies were referenced to the C 1s peak at 284.6 eV, which was applied as an internal standard. Oxygen defects were examined by electron paramagnetic resonance (EPR) with Bruker A300-10 at 77K. The synchrotron-based X-ray absorption spectroscopy (XAS) was measured at the beamline 1W1B station of Beijing Synchrotron Radiation Facility (BSRF). The obtained XAFS data was processed in Athena (version 0.9.26) for background, pre-edge line and post-edge line calibrations. For Wavelet Transform analysis, the $\chi(k)$ exported from Athena was imported into the Hama Fortran code. The parameters were listed as follow: R range, 1-6 Å, k range, 0-12 $Å^{-1}$ for samples; k weight, 2; and Morlet function with $\kappa=10$, $\sigma=1$ was used as the mother wavelet to provide the overall distribution. *In-situ* electrochemical Raman measurement was performed with a home-designed electrochemical cell and a HORIBA Raman microscope equipped with a 532 nm laser and a 50× objective lens. The grating parameter was 600 (750 nm), and the laser intensity was 10%. The catalysts tested for stability was mechanically detached from the working electrode, washed thoroughly with ethanol via repeated procedure of dispersion, ultrasonication, and centrifugation to remove Nafion and finally dried for TEM and XPS characterizations.

Electrochemical measurements.

The electrochemical measurements were carried out on an CHI760E electrochemical station at room temperature. The glassy carbon loaded with catalysts (GC, diameter: 3 mm), silver chloride (Ag/AgCl in saturated KCl), and graphite rod were used as working electrode, reference electrode, and counter electrode, respectively. For all the electrochemical measurements, 0.5 M H_2SO_4 aqueous solution was used as the electrolyte. The Ag/AgCl electrode was calibrated with respect to the RHE by measuring the polarization curve of Pt electrode in highly pure H_2-saturated 0.5 M H_2SO_4 electrolyte (Figure S12). All the potentials shown in our tests were calibrated and transformed to $E(\mathrm{RHE}) = E(\mathrm{Ag/AgCl}) + 0.207$ V for acidic conditions. The catalyst ink was made by dispersing 5 mg electrocatalyst into solvent containing 0.96 mL ethanol and 0.04 mL 5 wt% Nafion solution and ultrasonicating for 1 h to ensure a homogeneous suspension. Later, 10 µL catalyst ink was drop-casted evenly onto the GC electrode and left naturally dried at room temperature. On the other hand, 200 µL of the catalyst ink was sequentially pipetted onto a piece of clean carbon cloth (CC, 1 cm × 1 cm), which was subjected to overnight solvent evaporation in air and then used as the working electrode. All the chronopotentiometry stability tests were evaluated in 0.5 M H_2SO_4 using a standard three electrode system with carbon cloth or glassy carbon electrode. The linear sweep voltammetry (LSV) with the scan rate of 5 mV s^{-1} was performed in the N_2-saturated 0.5 M H_2SO_4 solution. Tafel slope was determined by plotting the overpotential versus the logarithm of current density (log |J|). Cyclic voltammetry (CV) was conducted at a scan rate of 1 mV s^{-1}. The electrochemical impedance spectroscopy (EIS) was conducted over the frequency range of 0.01-10^5 kHz with an amplitude of 10 mV. *In situ* EIS was carried out at the specified potential to obtain the surface chemical composition and structural information of the materials. For the pH-dependent activity measurement, 0.05, 0.16 and 0.5 M H_2SO_4 solution (pH = 1.0, 0.5, 0, respectively. Measured by a Horiba D-71 pH meter) was used as electrolyte without adding buffer salt. The electrochemical double-layer capacitance (C_{dl}) measurements were obtained at non-faradaic potentials by recording cyclic voltammetry at different scan rates (40, 60, 80, 100, 120, 140 and 160 mV s^{-1}). An two-eletrode stsyem was empomed to carry out overall water-splitting in 0.5 M H_2SO_4, using 20% Pt/C and Sm-RuO_{2-x}-O_v both dropped on carbon cloth as the cathode and anode,seperately

ICP analysis of the Ru dissolution

The dissolution of catalysts during the OER process at 10 mA cm^{-2} in a total volume of 50 mL electrolyte was quantified by inductively coupled plasma optical emission spectrometry (ICP-MS Elan DRC-e). A volume (10 mL) of electrolyte was used to fulfill the limit of detection of the equipment. The electrolyte for Sm-RuO_{2-x}-O_v was sampled after 320 h electrolysis, while the electrolyte for pure RuO_2 was sampled after 10 h electrolysis.

In situ Raman spectroscopy

The *in-situ* Raman measurements were carried out in an *in-situ* Raman cell equipped with a three-electrode system. Simultaneous acquisition of multipotential Raman spectra while catalyst OER procedure in 0.5 M H_2SO_4. Raman spectra were recorded from 200 cm^{-1} to 1000 cm^{-1} by a LabRAM HR 800 Raman spectrometer with an excitation laser of 532 nm.

Tetramethylammonium cation (TMA^+) measurement

To study the mechanism of the water oxidation reaction, two types of 0.5 M solutions were prepared by using 0.5 M H_2SO_4 and $(CH_3)_4NSO_4$ Milli-Q water (fixing c[$(CH_3)_4NSO_4$] = 0.1 M if used), separately. All vessels were cleaned with Milli-Q water carefully and dried under an infrared lamp for over 1 hour before use removing the influence of normal H_2O, and the catalyst-coated electrodes were soaked in the electrolyte solution for 30 mins before electrochemical experiments to make sure to reach the H-D exchange equilibrium. The electrochemical experiments were conducted using the same procedures described before.

Turnover frequency (TOF)

TOF for catalysts was measured in a three-electrode system with glassy carbon as the working electrode. TOF is defined as the frequency of reaction per active site, to compare the intrinsic activity of different catalysts. TOF was computed from:

$$TOF\ (O_2\, s^{-1}) = \frac{Total\ \ oxygen\ turnover\ per\ geometric\ area}{Activite\ sites\ per\ geomenteric\ area}$$

The total number of hydrogen turnovers was calculated from the current density using the Formula:

$$Total\ \ oxygen\ turnover\ per\ geometric\ area:$$
$$= \left[j\ (mA\ cm^{-2})\right]\left[\frac{1\ (C\ s^{-1})}{10^3\ (mA)}\right]\left[\frac{1\ (mol\ e^{-1})}{96485.3\ (C)}\right]\left[\frac{1\ (mol\ O_2)}{4\ mol\ e^{-1}}\right]\left[\frac{6.023\ \times 10^{23}\ molecules\ O_2}{1\ mol\ O_2}\right]$$
$$= 1.56\ \times 10^{15}\ O_2\, s^{-1}\, cm^{-2}\ per\ mA\ cm^{-2}$$

The number of active sites in Sm-RuO_{2-x}-O_v catalyst was calculated from the total mass of Ru on the electrode and the atomic weight of Ru, if all Ru atoms contributed to the reaction process:

$$Activite\ sites\ per\ geomenteric\ area: = \frac{Catalysts\ loading\ mass\ \ \times Ru\ mass\ precentage\ \ \times 6.023\ \times 10^{23}}{101.07\ g\ mol^{-1}}$$

All Ru atoms were assumed as active sites, computed based on ICP-MS findings.

Specific area activity (SA)

The specific area activity was determined by normalizing the ECSA for different catalysts. The specific current density per ECSA (j_{ECSA}) was computed from:

$$j_{ECSA} = \frac{j_{geo} \times A_{geo}\ \times\ C_s}{C_{dl}}$$

where j_{geo} is the geometric area current density and A_{geo} the geometric area of the glassy carbon electrode (0.0706 cm^{-2}). C_{dl} was measured from CV. The C_s for 0.04 $mF\ cm^{-2}$ was used to estimate ECSA.

Mass activity (MA)

The Mass activity for catalysts was measured based on data obtained from the three-electrode system with glassy carbon as the working electrode. Mass activity is used to compare the intrinsic activity of different catalysts. Mass activity was computed from:

$$MA = \frac{Current\ density\ per\ mA\ cm^{-2}}{catalyst\ mass\ loading\ per\ geomenteric\ area}$$

Calculation methods

All the spin-polarized density functional theory (DFT) calculations were performed via Vienna ab initio Simulation Package (VASP).[1, 2] The Perdew-Burke-Ernzerhof (PBE) functional under general gradient approximation (GGA) method was selected.[3] The projector augmented-wave (PAW) method was used to describe the interactions between ions and electrons.[4] The cut-off energy for the plane-wave basis was set to be 450 eV. The convergence criterion for all forces was set to be lower than 0.2 eV nm^{-1}. The convergence for the electronic self-consistence was lower than 10^{-5} eV. To deal with the strongly on-site coulombic interaction from localized 3d and 4f electrons, the Hubbard U correction by Dudarev et al.[5] was introduced by considering the effective U value Ueff, where 2.0 eV and 6.0 eV are adopted for Ru-3d and Sm-4f electrons respectively according to previous works.[6, 7] For other REs calculated in this work, including Nd and Lu, the DFT + U scheme was also considered as similar to Sm. The k-mesh for the first Brillouin zone was 3 × 3 × 3 based on the Gamma-center sampling toward the bulk structure. For slab model, the Monkhorst-Pack k-points integration was 2 × 2 × 1. For geometric optimization, the vacuum layer chose 1.5 nm to avoid the self-interactions between the periodically repeated slabs. The RE-RuO_2 models is based on the RuO_2 (110) surface by replacing the surface Ru with RE.[8] For each oxygen intermediate, the free energy can be calculated as $G = E + ZPE - TS$, where E stands for the total energy, ZPE is the zero-point energy, T is the absolute temperature, and S represents the entropy. The bias potential acted on the free energy of e^- can be treated as $\Delta G(U) = -eU_{RHE}$, where U_{RHE} is the electrode potential versus reversible hydrogen electrode.

.

Figures and tables

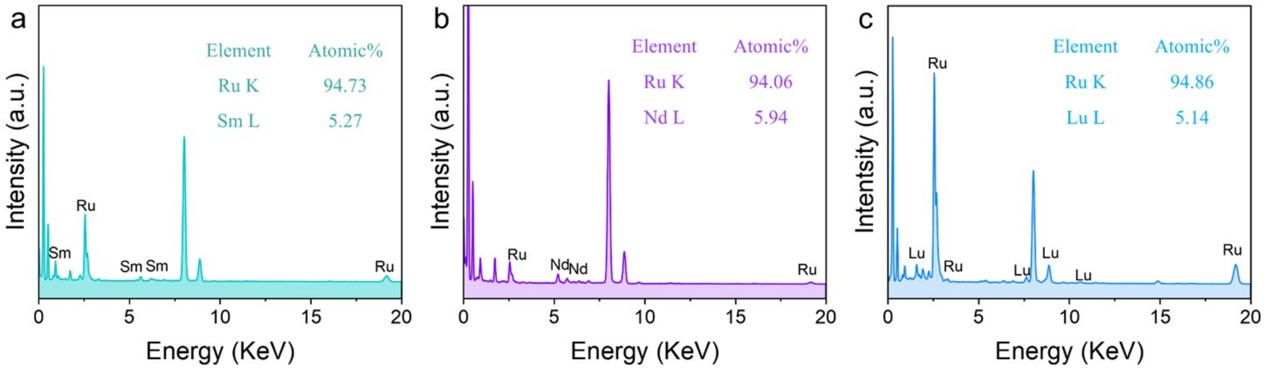

Figure S1. EDX spectra of different RE-RuO_{2-x}-O_v samples.

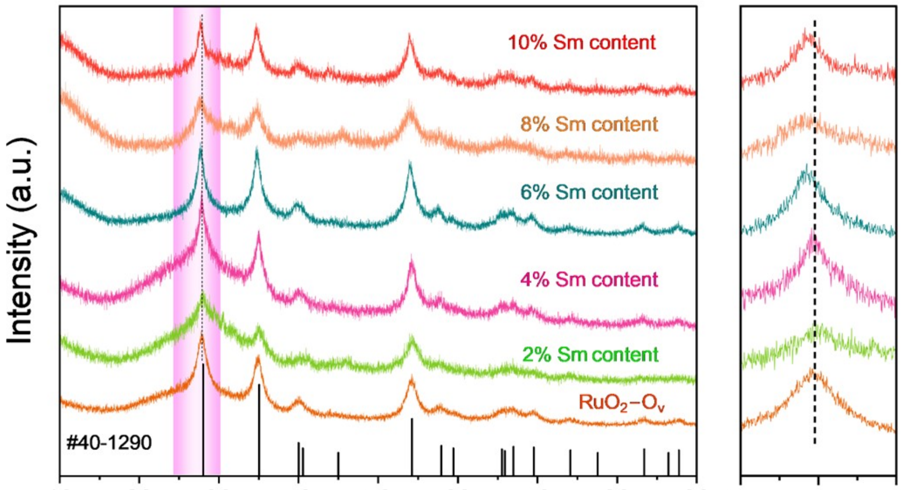

Figure S2. XRD patterns of Sm-RuO_{2-x}-O_v with various Sm contents.

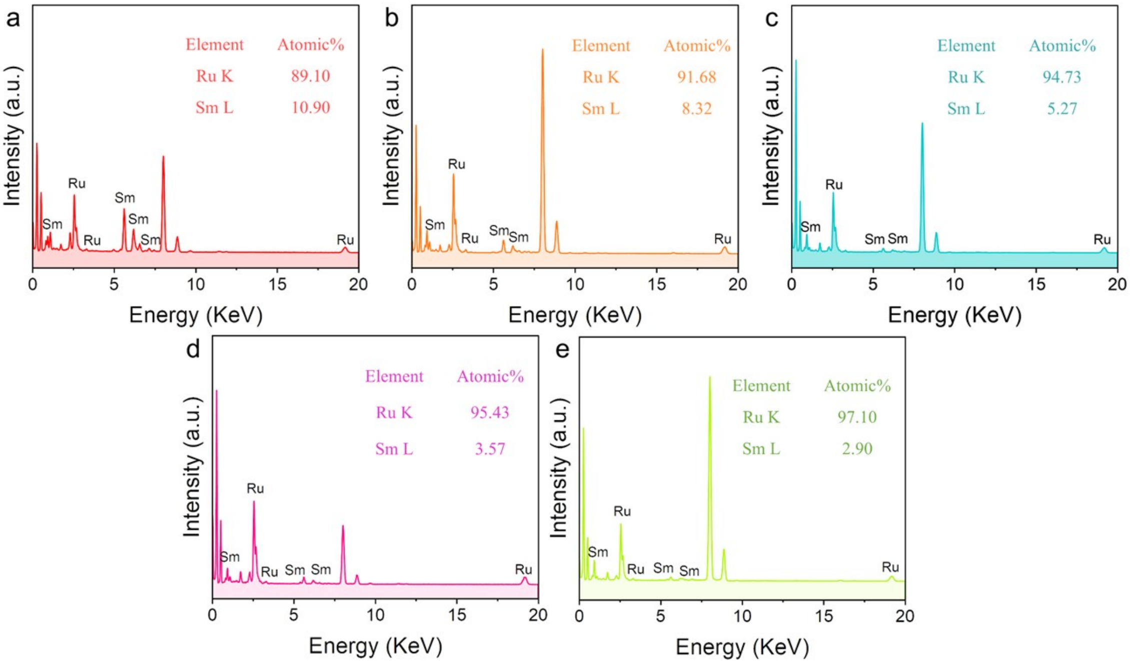

Figure S3. EDX spectra of Sm-RuO_{2-x}-O_v with various Sm contents.

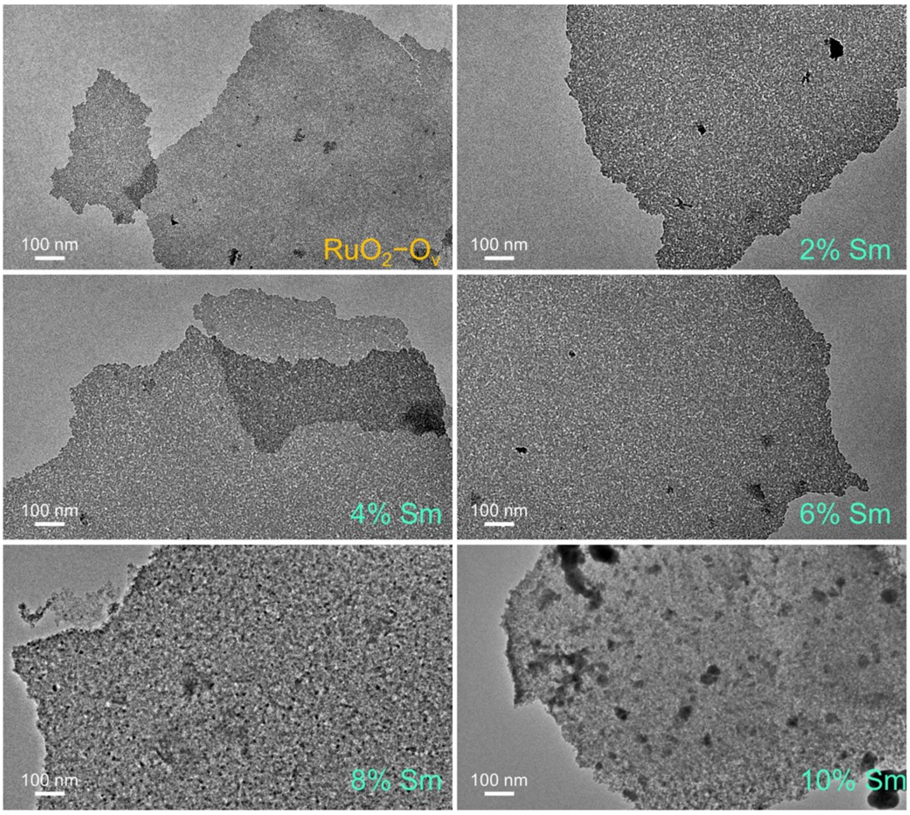

Figure S4. TEM images of Sm-RuO_{2-x}-O_v with various Sm contents.

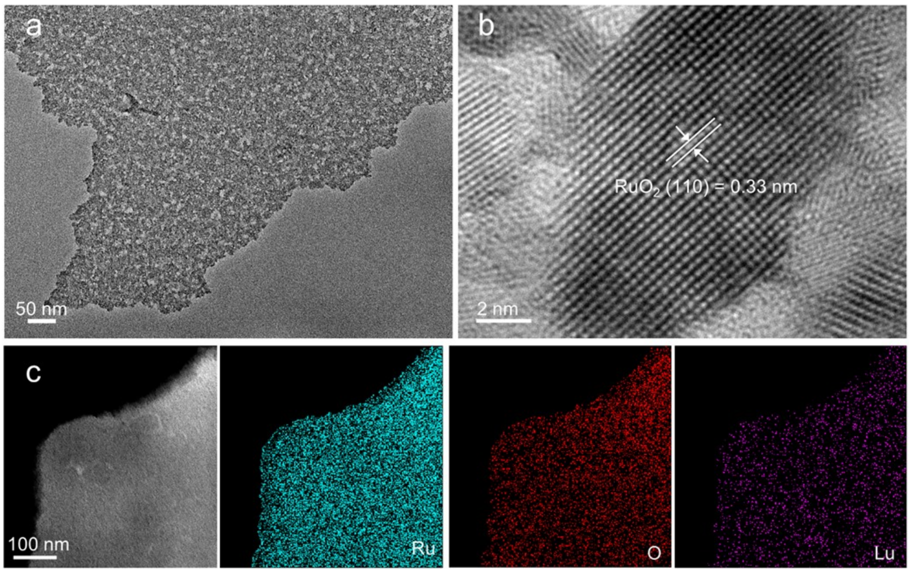

Figure S5. Morphological characterizations of Lu-RuO_{2-x}-O_v. (a-b) TEM and HRTEM images. (c) HAADF-STEM image and corresponding EDS elemental mapping.

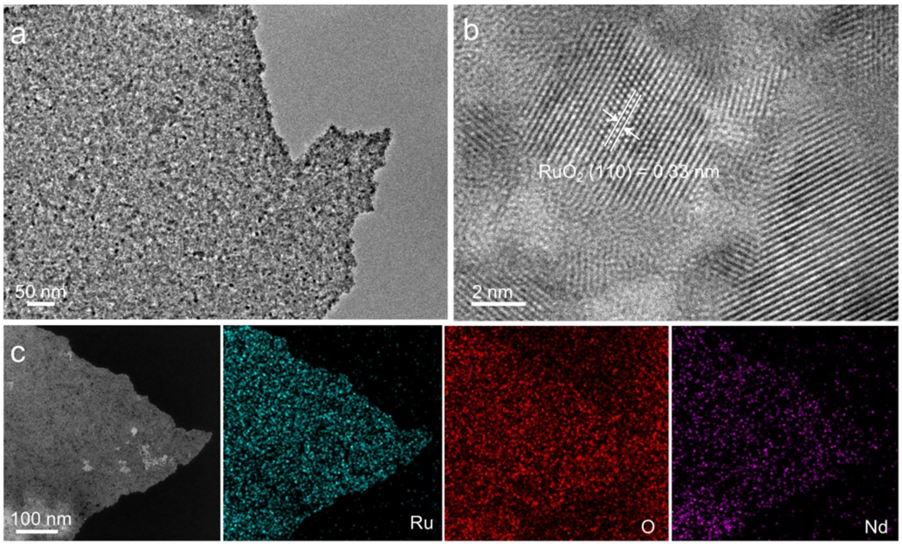

Figure S6. Morphological characterizations of Nd-RuO_{2-x}-O_v. (a-b) TEM and HRTEM images. (c) HAADF-STEM image and corresponding EDS elemental mapping.

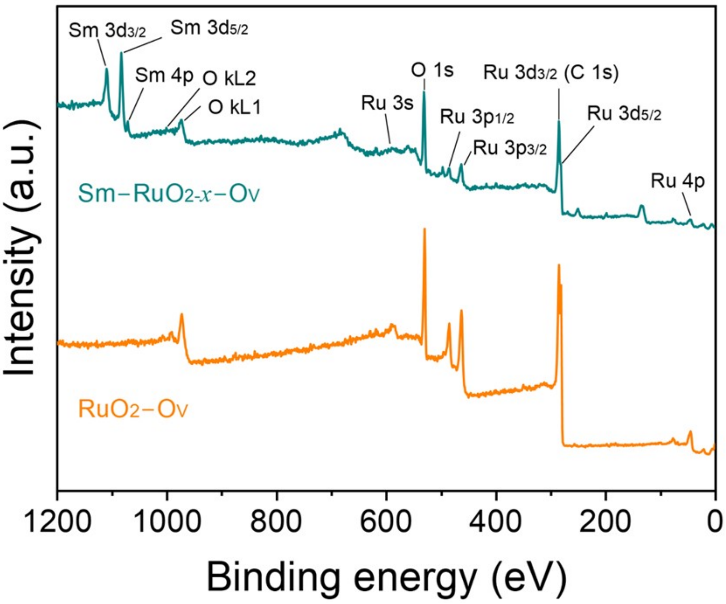

Figure S7. XPS scanning spectra of Sm-RuO_{2-x}-O_v and RuO_2-O_v.

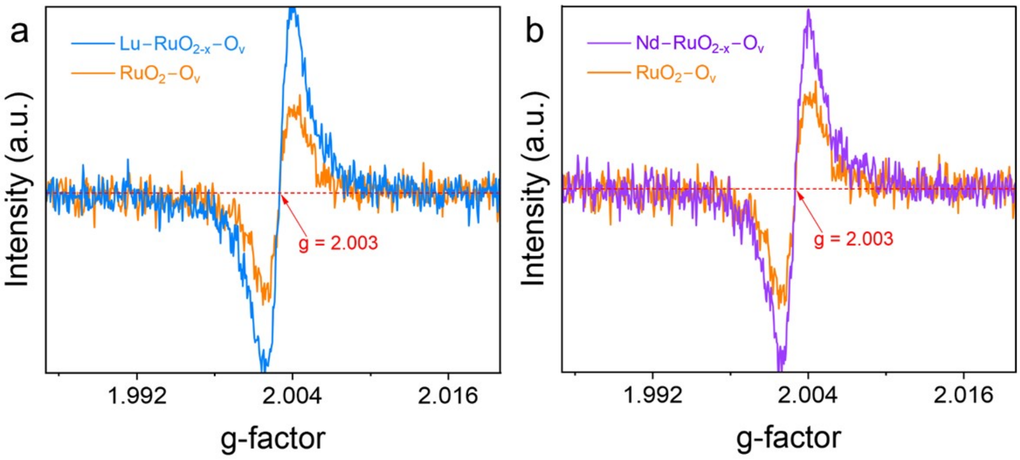

Figure S8. EPR spectra of Lu-RuO_{2-x}-O_v, Nd-RuO_{2-x}-O_v and RuO_2-O_v.

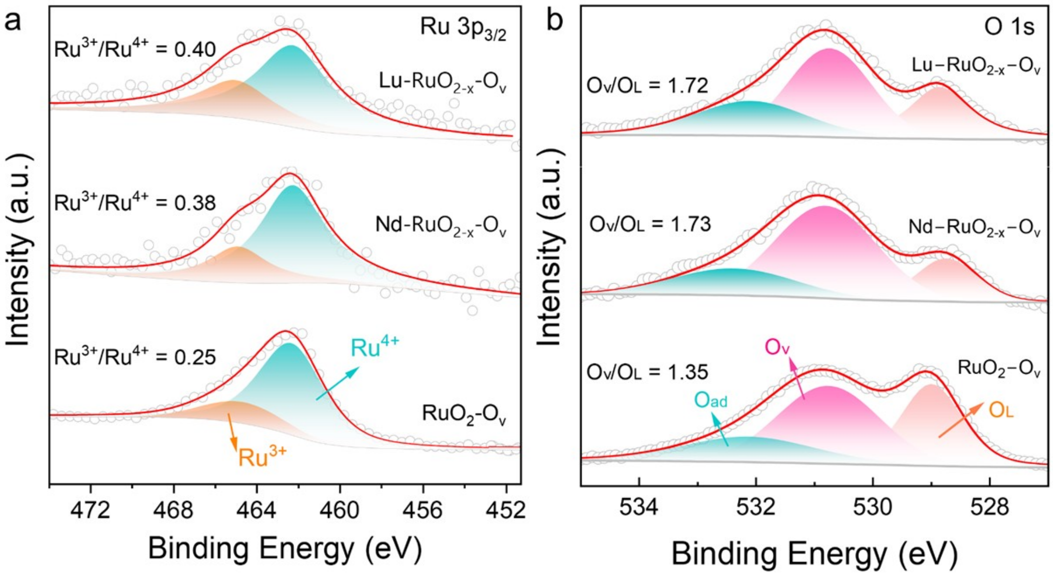

Figure S9. Comparisons of (a) Ru $3p_{3/2}$ and (b) O 1s XPS spectra of Lu-RuO_{2-x}-O_v, Nd-RuO_{2-x}-O_v and RuO_2-O_v, respectively.

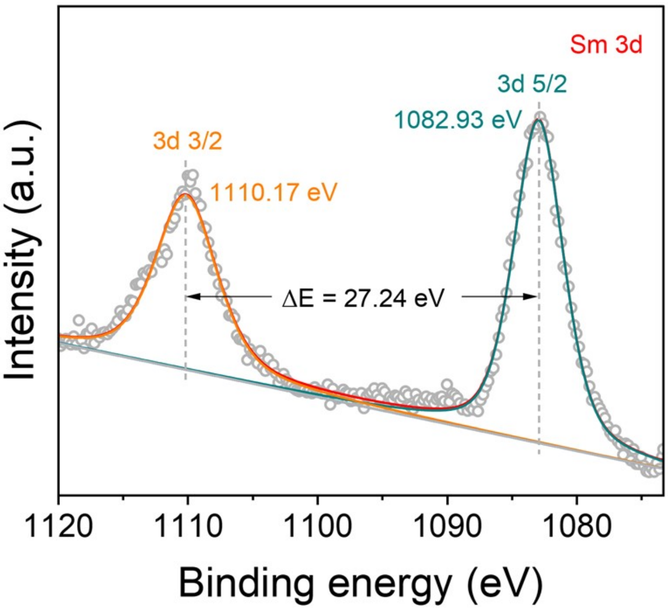

Figure S10. Sm 3d core level XPS spectrum for Sm-RuO_{2-x}-O_v.

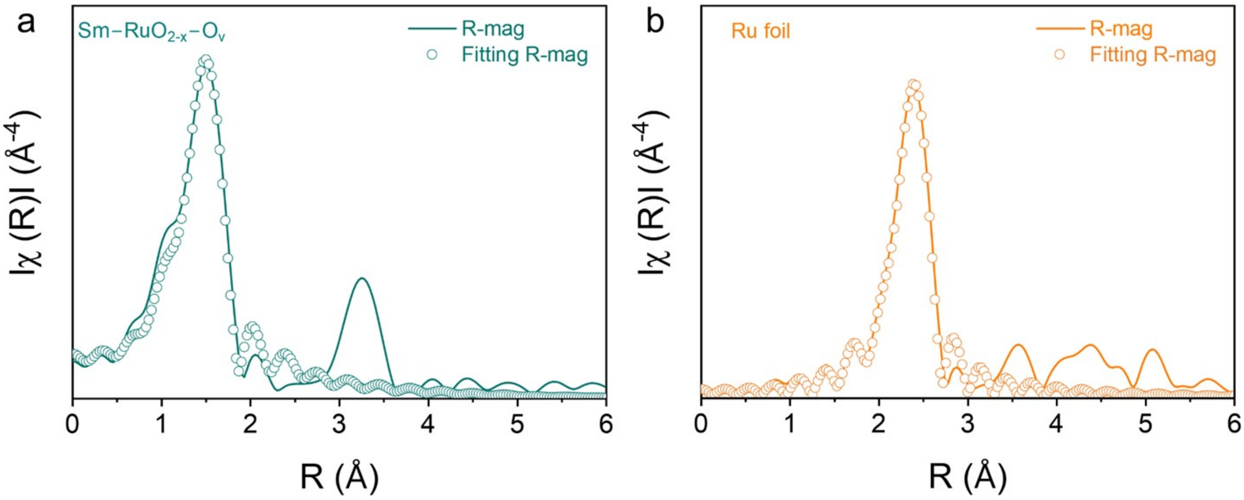

Figure S11. First shell fitting in R space of EXAFS for (a) Sm-RuO$_{2-x}$-O$_v$ and (b) Ru foil.

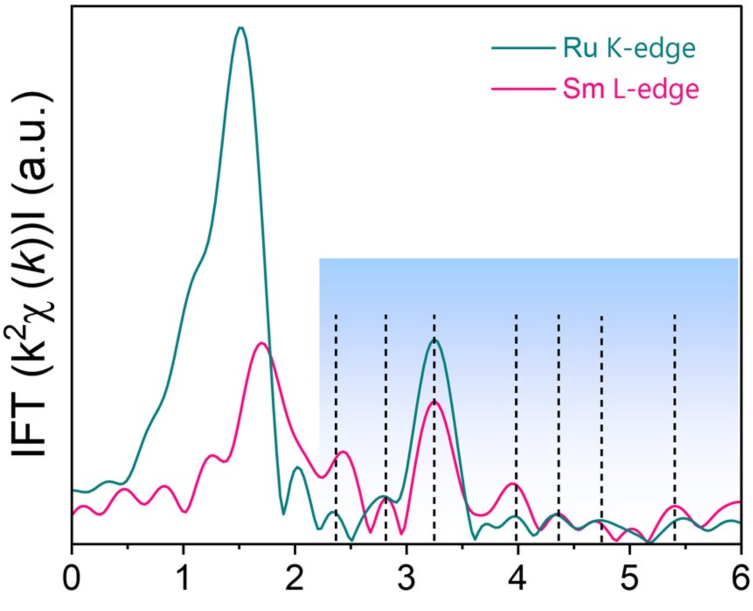

Figure S12. Comparation of Fourier transformed Sm and Ru K-edge EXAFS of Sm-RuO$_{2-x}$-O$_v$.

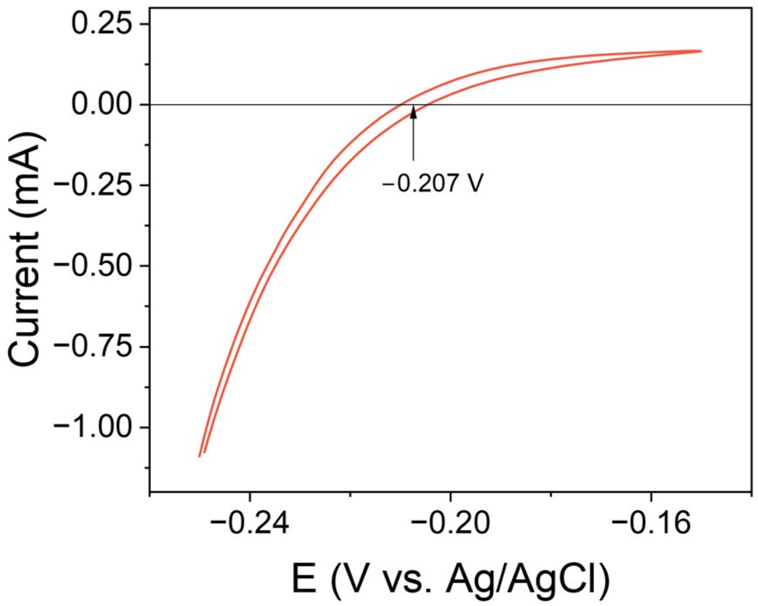

Figure S13. LSV curve for the calibration of Ag/AgCl electrode in 0.5 M H_2SO_4 electrolyte with H_2 saturation. Commercial Pt/C, Ag/AgCl, and Pt plate were used as working, reference, and counter electrodes, respectively. scan rate: 1 mV s^{-1}.

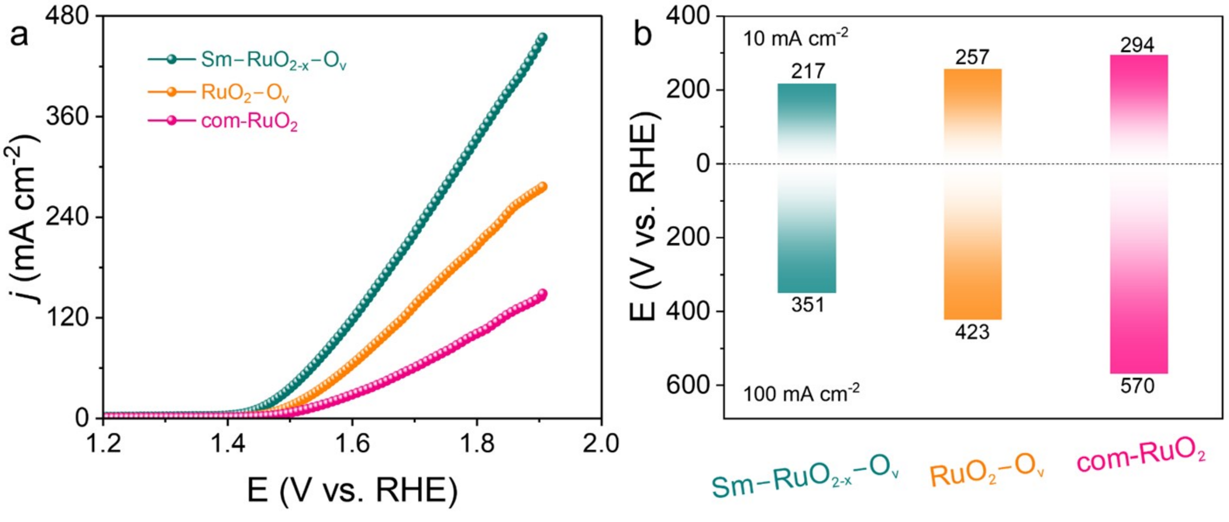

Figure S14. (a) LSV curves for Sm-RuO_{2-x}-O_v, RuO_2-O_v and com-RuO_2 in 0.5 M H_2SO_4. (b) Corresponding comparison of overpotential at 10 mA cm^{-2} and 100 mA cm^{-2}, respectively.

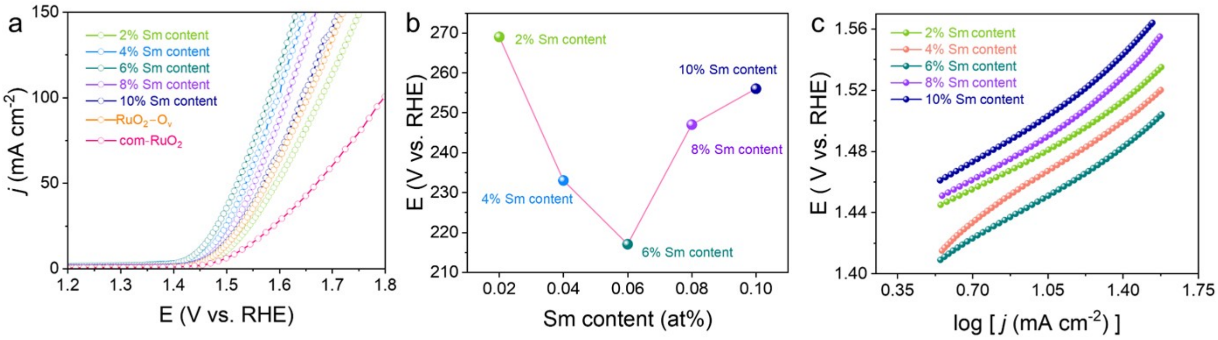

Figure S15. (a) LSV curves for RuO$_2$-O$_v$, com-RuO$_2$ and Sm-RuO$_{2-x}$-O$_v$ with various Sm content. (b) The relationship between activity and Sm content. (c) Tafel plots of RuO$_2$-O$_v$, com-RuO$_2$ and Sm-RuO$_{2-x}$-O$_v$ with various Sm content.

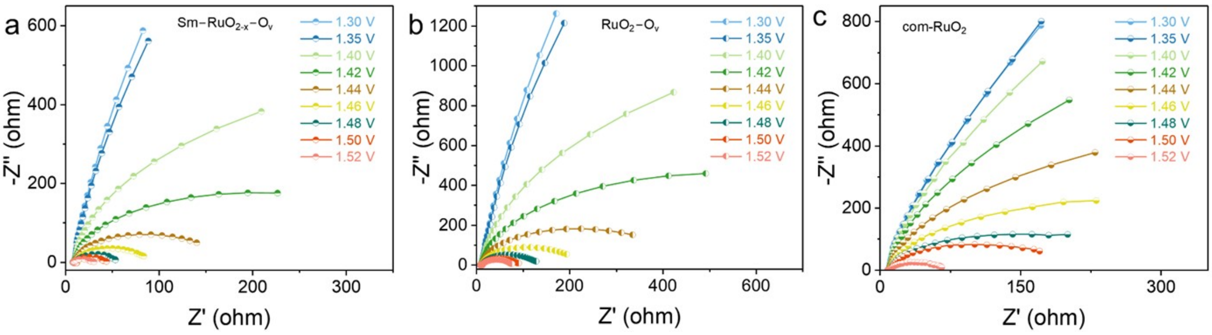

Figure S16. Nyquist plots for Sm-RuO$_{2-x}$-O$_v$, RuO$_2$-O$_v$ and com-RuO$_2$ in 0.5 M H_2SO_4.

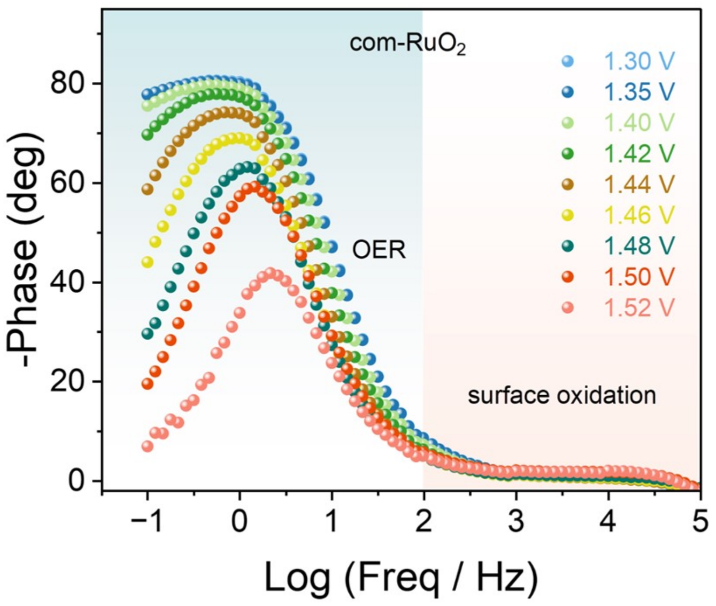

Figure S17. Bode phase plots of com-RuO_2 in 0.5 M H_2SO_4.

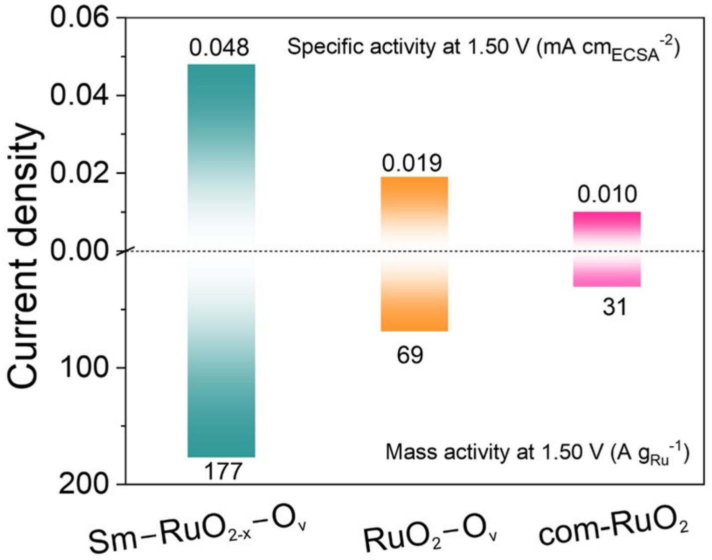

Figure S18. The comparation of mass activity and specific activity at 1.50 V.

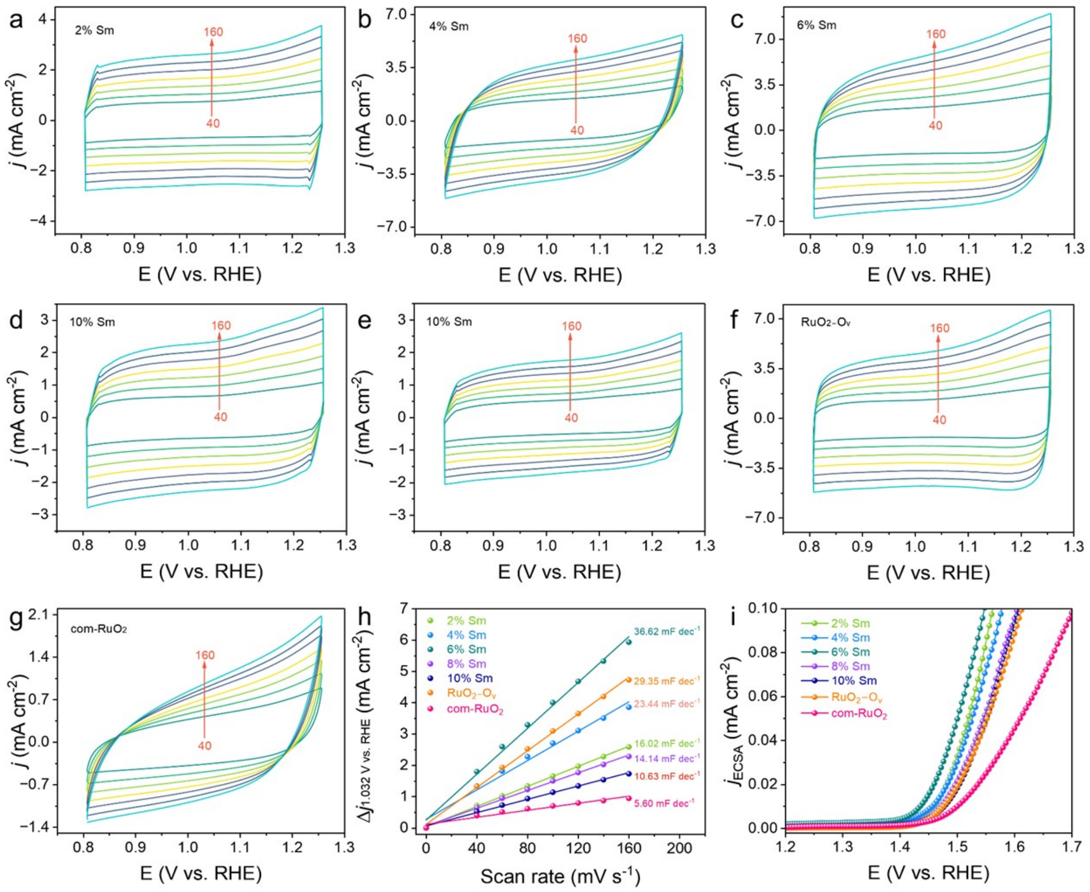

Figue S19. CV profiles of Sm-RuO$_{2-x}$-O$_v$ with various Sm content (a) 2%Sm; (b) 4%; (c) 6%; (d) 8%; (e) 10%. (f) RuO$_2$-O$_v$. (g) com-RuO$_2$. (h) C_{dl} plots derived from the fitting CV curves at different scan rates. (i) Intrinsic activity normalized on ECSA.

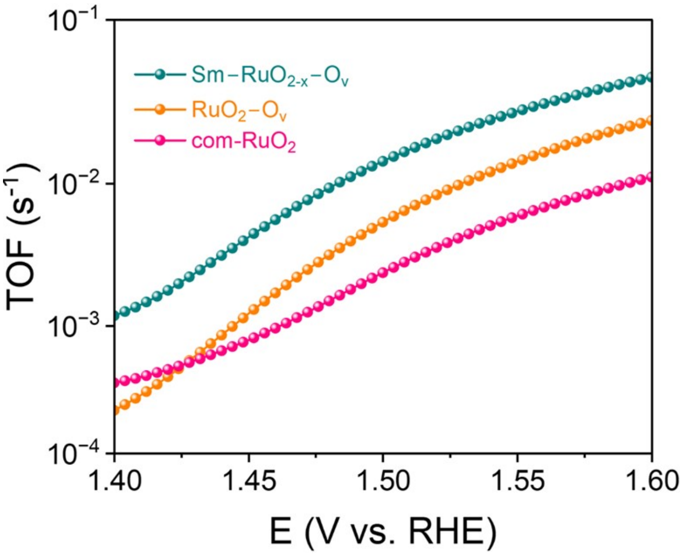

Figure S20. Turnover frequency curves of Sm-RuO$_{2-x}$-O$_v$, RuO$_2$-O$_v$ and com-RuO$_2$.

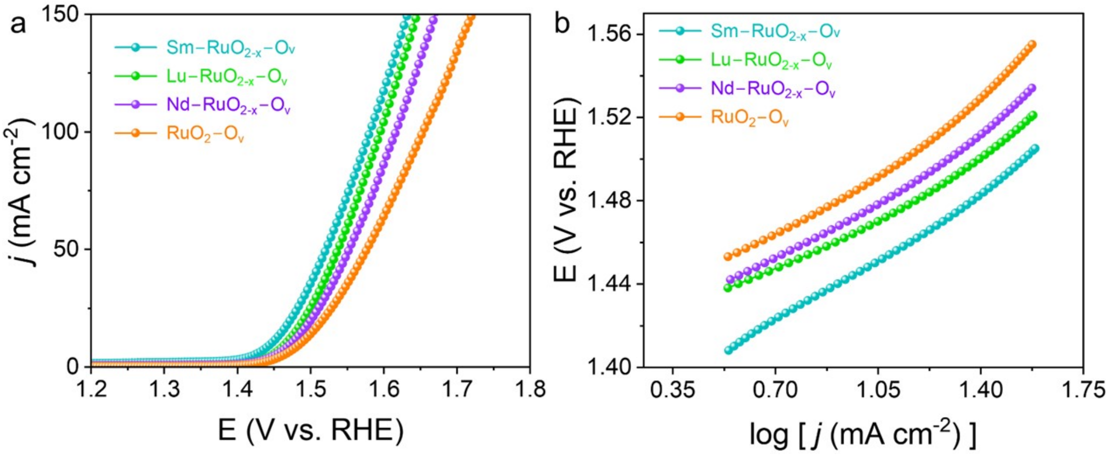

Figure S21. (a) LSV curves and (b) Tafel plots of RuO_2-O_v and RE-RuO_{2-x}-O_v.

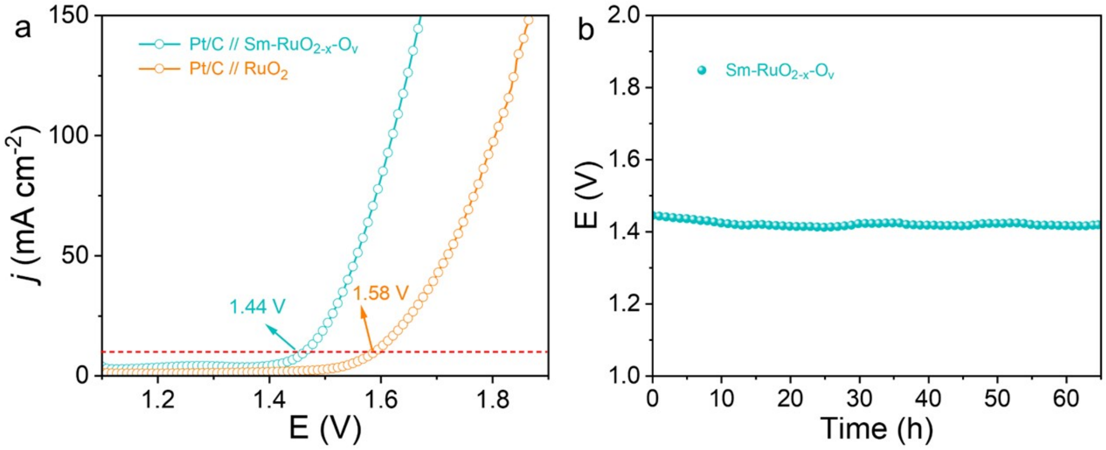

Figure S22. (a) Chrono-voltammetry curves for Pt/C // Sm-RuO_{2-x}-O_v and Pt/C // RuO_2 electrolytic cells. (b) Time-potential curve of Pt/C // Sm-RuO_{2-x}-O_v electrolyzer.

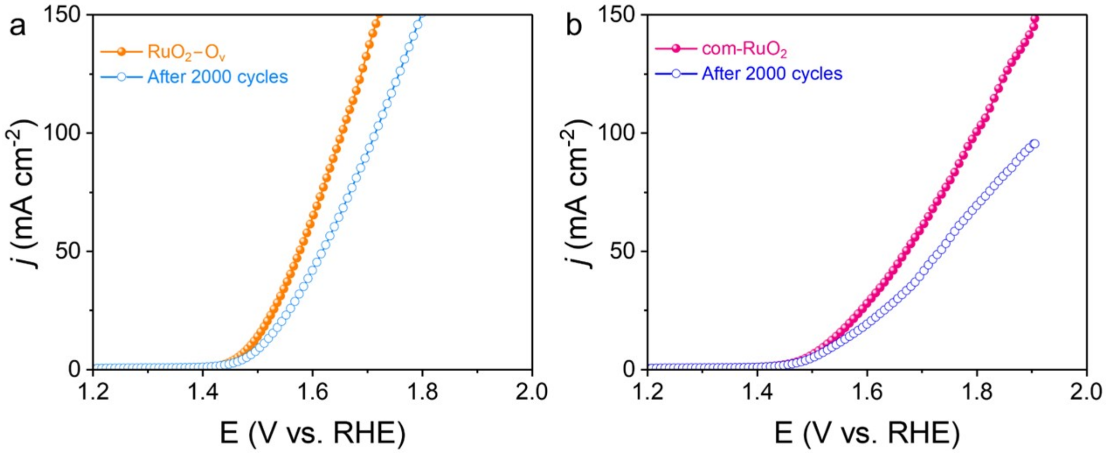

Figure S23. (a) Polarization curves of RuO_2-O_v before and after 2000 CV cycles. (b) Polarization curves of com-RuO_2 before and after 2000 CV cycles.

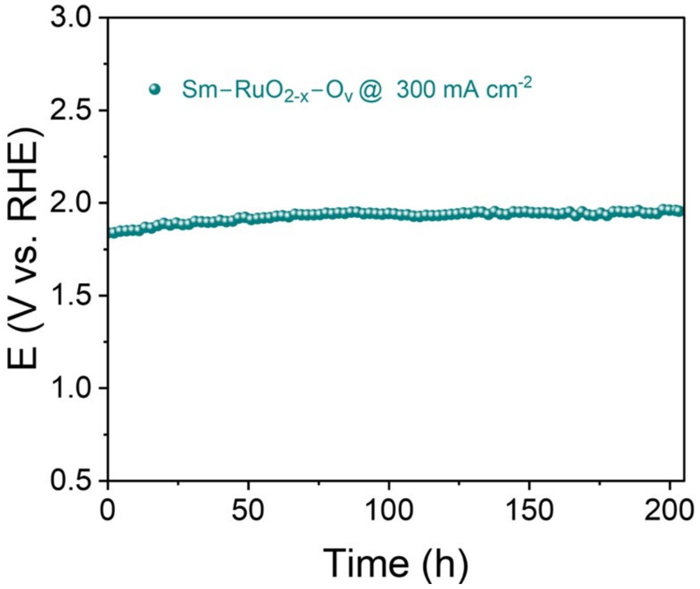

Figure S24. Chronopotentiometry measurement of Sm-RuO_{2-x}-O_v at the current density of 300 mA cm^{-2}.

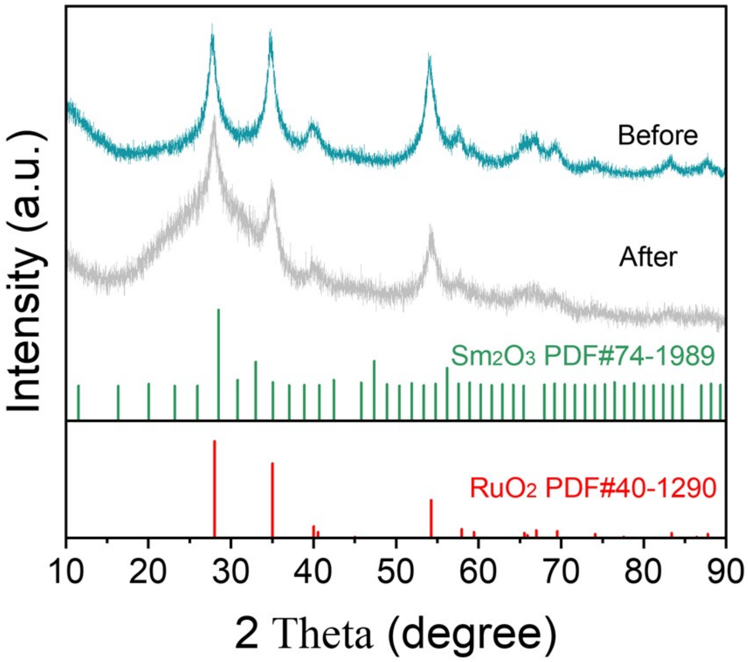

Figure S25. Comparison of XRD patterns of Sm-RuO_{2-x}-O_v before and after a 320 hour stability test.

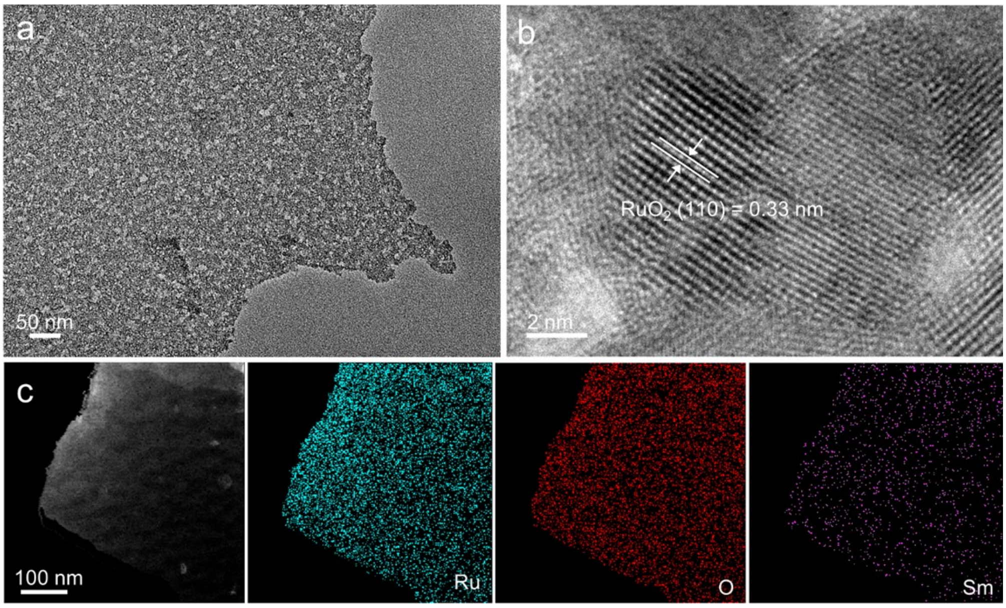

Figure S26. Morphology and surface structural characterizations of Sm-RuO_{2-x}-O_v after the OER stability test at 10 mA cm^{-2} for 320 h. (a, b) TEM and HRTEM images. (c) HAADF-STEM images and corresponding EDS elemental mapping.

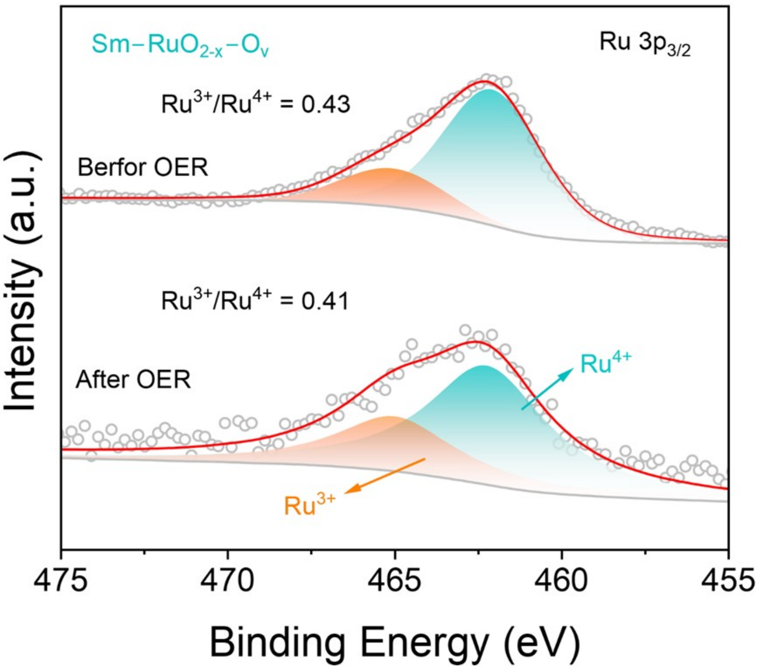

Figure S27. Ru 3p XPS spectra of Sm-RuO_{2-x}-O_v before and after the OER stability test at 10 mA cm^{-2} for 320 h.

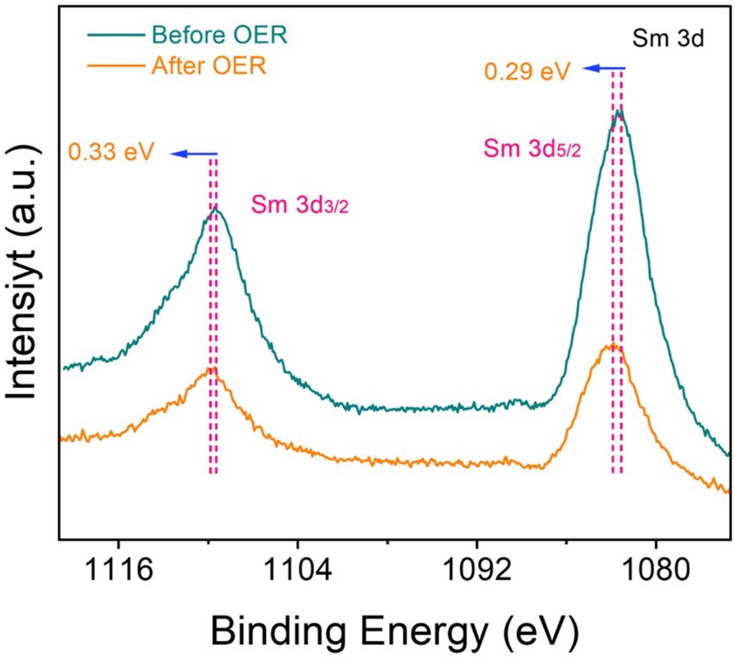

Figure S28. Sm 3d XPS spectra of Sm-RuO_{2-x}-O_v before and after the OER stability test at 10 mA cm^{-2} for 320 h.

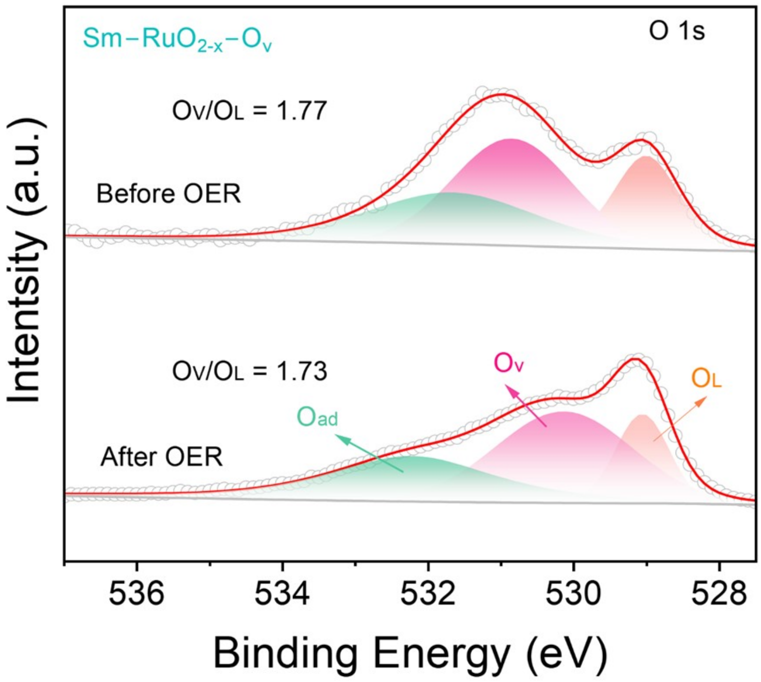

Figure S29. O 1s XPS spectra of Sm-RuO$_{2\text{-x}}$-O$_v$ before and after the OER stability test at 10 mA cm^{-2} for 320 h.

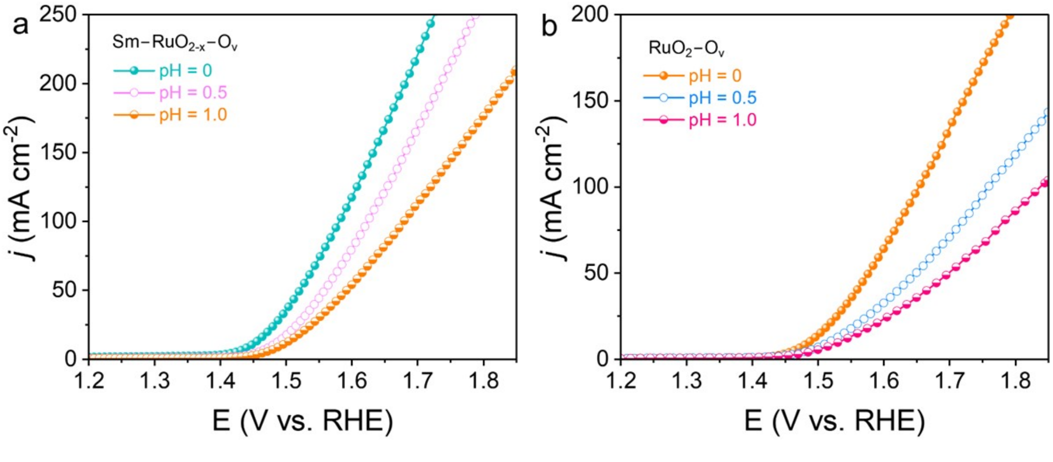

Figure S30. pH dependence of OER performance of (a) Sm-RuO$_{2\text{-x}}$-O$_v$ and (b) RuO$_2$-O$_v$ under H$_2$SO$_4$ (pH values: 0, 0.05 and 1.0, respectively).

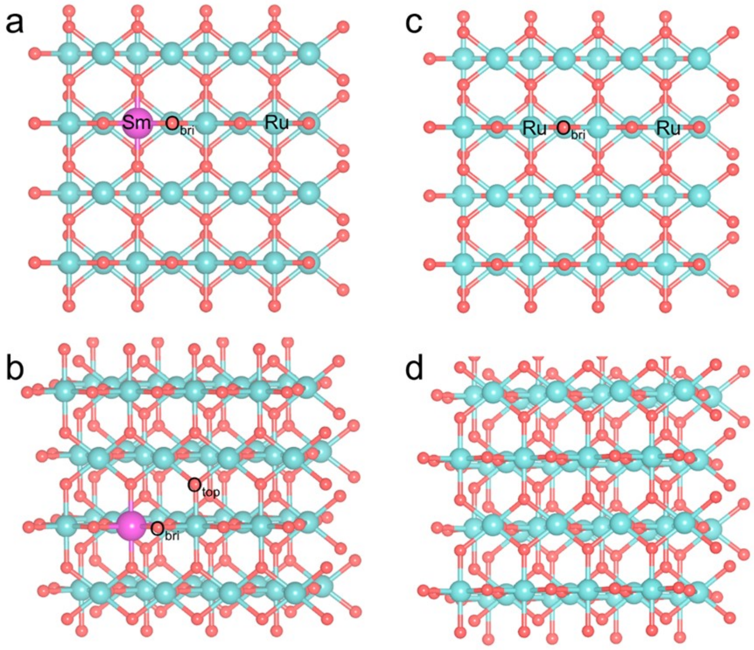

Figure S31. Optimized structures of (a, b) $Sm-RuO_2$ model and (c, d) RuO_2 model.

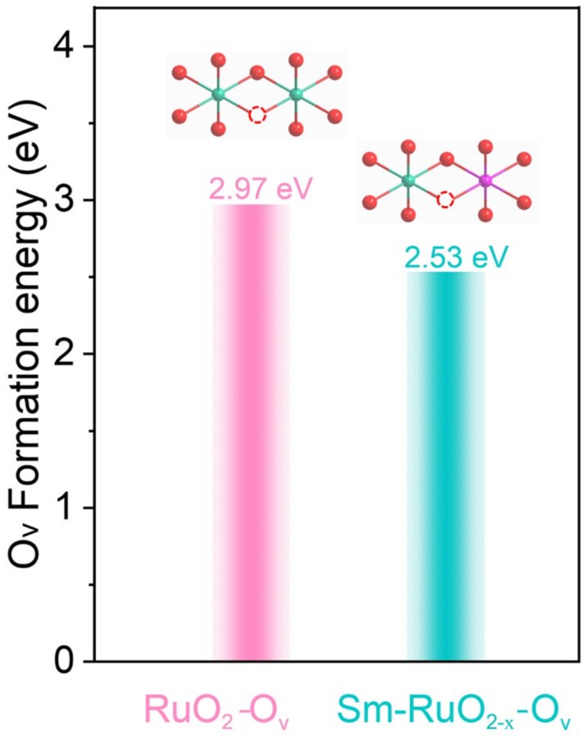

Figure S32. The formation energy of bridge O_v defects $Sm-RuO_2$ model and RuO_2-O_v respectively.

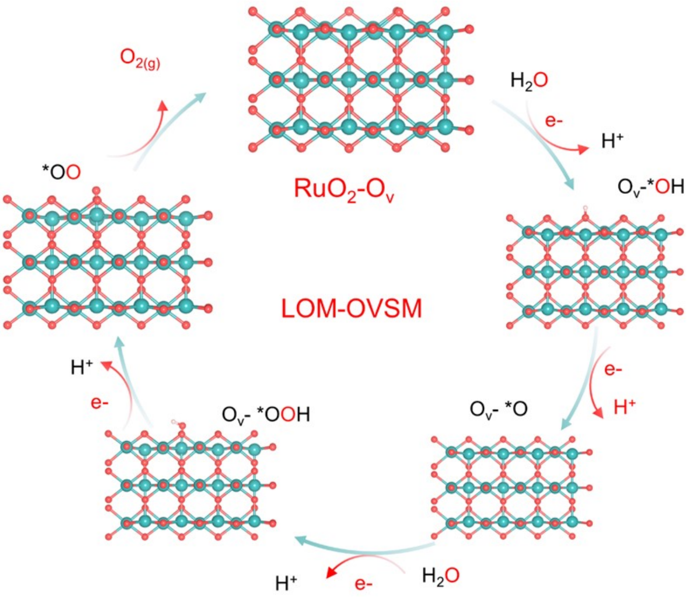

Figure S33. Schematic illustration for RuO_2-O_v proceed LOM-OVSM pathway.

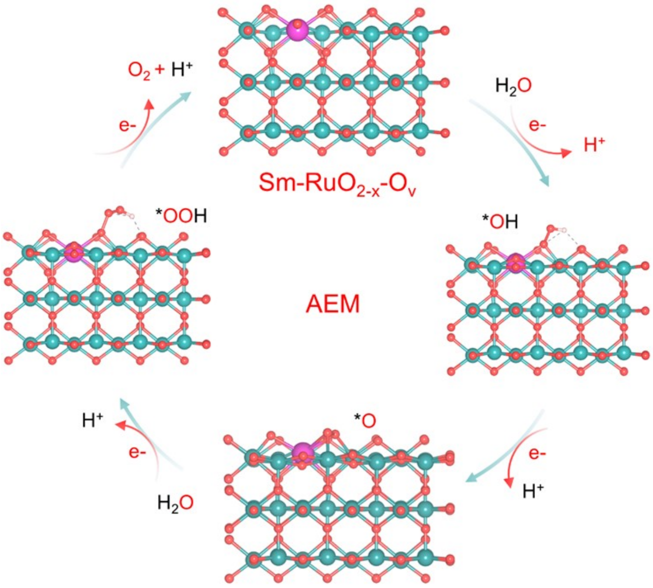

Figure S34. Schematic illustration for Sm-RuO_{2-x}-O_v proceed AEM pathway.

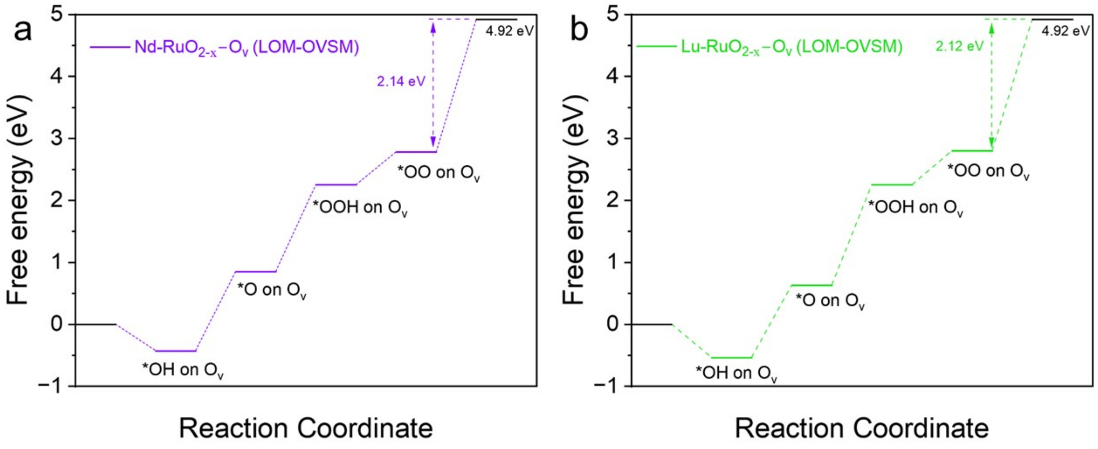

Figure S35. Gibbs free energy illustration for (a) Nd-RuO$_{2-x}$-O$_v$ and (b) Lu-RuO$_{2-x}$-O$_v$ during OER by LOM-OVSM pathways.

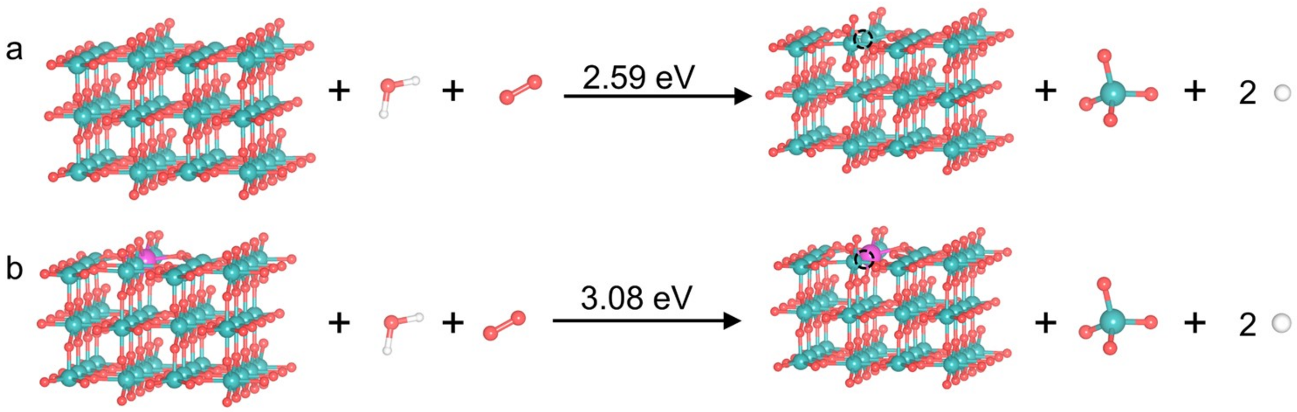

Figure S36. Atomistic structures showing the demetallation of Ru from (a) RuO$_2$-O$_v$ (110) surface, and (b) Sm-RuO$_{2-x}$-O$_v$ (110) surface. In the figure, the green, red, white and purple balls represent Ru, O, H and Sm atoms, respectively. Black circles represent Ru vacancy. Here, using H_2O and O_2 as oxidants and RuO_4 as the final dissolution product. A high value of the calculated enthalpy change for this proposed process represents high stability against the demetallation of Ru.

Table S1. ICP-MS results of RE-RuO$_{2-x}$-O$_v$ catalysts.

Samples	RE (at%)	Ru (at%)
Sm-RuO_{2-x}-O_v	6.17%	93.83%
Nd-RuO_{2-x}-O_v	6.54%	93.46%
Lu-RuO_{2-x}-O_v	6.26%	93.73%
RuO_2-O_v	/	95.4%
Commercial RuO_2	/	95.9%

Table S2. EXAFS fitting parameters at the Ru K-edge for various samples（S_0^2=0.85 from Ru-foil）

Samples	Path	CN^a	R^b(Å)	σ^{2c}(Å^2)	$\Delta E_0{}^d$(eV)	R factor (%)
Ru-foil	Ru-Ru	12	2.67±0.01	0.0034±0.0004	2.02±0.67	1.3
Sm-RuO_{2-x}-O_v	Ru-O	5.3±0.7	1.98±0.01	0.0025±0.0017	1.97±1.85	1.4

^{a}*CN*: coordination numbers; ^{b}*R*: bond distance; $^c\sigma^2$: Debye-Waller factors; ^{d} ΔE_0: the inner potential correction. R factor: goodness of fit. Error bounds that characterize the structural parameters obtained by EXAFS spectroscopy were estimated as CN±20%; R ± 1%; σ^2 ± 20%.

Table S3. Comparison of the acidic OER performance of Sm-RuO_{2-x}-O_v with recently reported Ru-based catalysts.

Catalysts	**Electrolyte**	**η_{10} (mV)**	**Tafel slope (mV dec^{-1})**	**Stability T(h) @ *j* (mA cm^{-2})**	**Ref.**
Sm-RuO_{2-x}-O_v	0.5 M H_2SO_4	217	45.76	320 h@10 mA cm^{-2} 100 h@100 mA cm^{-2} 200 h@300 mA cm^{-2}	**This work**
$SnRuO_x$	0.5 M H_2SO_4	176	38.2	250 h@10 mA cm^{-2}	9
$(Ru\text{-}W)O_x$	0.5 M H_2SO_4	170	46.2	300 h@10 mA cm^{-2}	10
Pt-RuO_2	0.5 M H_2SO_4	228	51	100 h@10 mA cm^{-2}	11
RuO_2/D-TiO_2	0.5 M H_2SO_4	180	43	100 h@10 mA cm^{-2}	12
La-RuO_2	0.5 M H_2SO_4	208	57.4	28 h@10 mA cm^{-2}	13
$Bi_{0.15}Ru_{0.85}O_2$	0.5 M H_2SO_4	200	59.6	100 h@10 mA cm^{-2}	14
Ga-RuO_2	0.5 M H_2SO_4	217.5	60.5	150 h@10 mA cm^{-2}	15
Ta-RuO_2	0.1 M $HClO_4$	201	55	280 h@10 mA cm^{-2}	16
$Re_{0.06}Ru_{0.9}4O_2$	0.1 M $HClO_4$	190	45.5	200 h@10 mA cm^{-2}	17
$Bi_xEr_{2-x}Ru_2O_7$	0.1 M $HClO_4$	180	51.3	100 h@10 mA cm^{-2}	18
RuO_2/MoO_3	0.5 M H_2SO_4	167	65	300 h@10 mA cm^{-2}	19
$La_{0.1}Ru_{0.9}O_2$	0.5 M H_2SO_4	188	76.6	60 h@10 mA cm^{-2}	20
$RuSnO_x$	0.1 M $HClO_4$	184	44.4	140 h@10 mA cm^{-2}	21
$W_{0.2}Er_{0.1}Ru_{0.7}O_{2-\delta}$	0.5 M H_2SO_4	168	66.8	500 h@10 mA cm^{-2}	22
$Nb_{0.1}Ru_{0.9}O_2$	0.5 M H_2SO_4	204	47.9	360 h@200 mA cm^{-2}	23
$Ba_{0.3}(SO_4)_\delta W_{0.2}Ru_{0.5}O_{2-\delta}$	0.5 M H_2SO_4	206	43.4	1000 h@10 mA cm^{-2}	24
$Ru_{0.8}Sb_{0.2}O_2$	0.5 M H_2SO_4	160	60.2	1100 h@10 mA cm^{-2}	25
$Ru_{0.6}Cr_{0.2}Ti_{0.2}O_x$	0.5 M H_2SO_4	238	58	1100 h@10 mA cm^{-2}	26
Er-RuO_x	0.5 M H_2SO_4	208	45	200 h@10 mA cm^{-2}	27
$Mn_{0.2}RuO_2$	0.5 M H_2SO_4	188	57	150 h@10 mA cm^{-2}	28
Bi-RuO_2	0.5 M H_2SO_4	192	37.84	650 h@10 mA cm^{-2}	29
$Ru_{0.5}Ir_{0.5}O_2$	0.5 M H_2SO_4	151	45	618 h@10 mA cm^{-2}	30

$Sr_{0.1}Ta_{0.1}Ru_{0.8}O_{2-x}$	0.5 M H_2SO_4	166	67.9	200 h@200 mA cm^{-2}	31
a-RuO_2@TM	0.5 M H_2SO_4	162	65.5	450 h@100 mA cm^{-2}	32

Table S4. ICP-MS data for Sm-$Ru_{2\text{-}x}$ O_v and RuO_2-O_v during stability measurement.

Time (h)	Dissolved Ru in Sm-$RuO_{2\text{-}x}$-O_v (ppb)	Dissolved Ru in Sm-$RuO_{2\text{-}x}$-O_v (ppb)	Time (h)	Dissolved Ru in RuO_2-O_v (ppb)
0.5	0.18	0.89	0.5	0.88
10	1.68	1.12	5	2.34
35	3.55	1.63	10	8.56
100	6.22	2.06	20	26.34
150	8.45	2.34	25	62.34
200	9.31	2.45	30	86.52
250	9.35	2.52	35	96.74
300	9.42	2.6	40	107.65

References

1. G. Kresse and J. Furthmüller, *Phys. Rev. B*, 1996, **54**, 11169-11186.
2. G. Kresse and J. Furthmüller, *Comput. Mater. Sci.*, 1996, **6**, 15-50.
3. J. P. Perdew, K. Burke and M. Ernzerhof, *Phys. Rev. Lett.*, 1996, **77**, 3865-3868.
4. G. Kresse and D. Joubert, *Phys. Rev. B*, 1999, **59**, 1758-1775.
5. S. L. Dudarev, G. A. Botton, S. Y. Savrasov, C. J. Humphreys and A. P. Sutton, *Phys. Rev. B*, 1998, **57**, 1505-1509.
6. M. Kuang, Y. Wang, W. Fang, H. Tan, M. Chen, J. Yao, C. Liu, J. Xu, K. Zhou and Q. Yan, *Adv. Mater.*, 2020, **32**, 2002189.
7. N. Batnyam, T. Ochirkhuyag and D. Odkhuu, *AIP Advances*, 2024, **14**, 035301.
8. D. Zhang, M. Li, X. Yong, H. Song, G. I. N. Waterhouse, Y. Yi, B. Xue, D. Zhang, B. Liu and S. Lu, *Nat. Commun.*, 2023, **14**, 2517.
9. Z. Shi, J. Li, Y. Wang, S. Liu, J. Zhu, J. Yang, X. Wang, J. Ni, Z. Jiang, L. Zhang, Y. Wang, C. Liu, W. Xing and J. Ge, *Nat. Commun.*, 2023, **14**, 843.
10. L. Deng, S.-F. Hung, Z.-Y. Lin, Y. Zhang, C. Zhang, Y. Hao, S. Liu, C.-H. Kuo, H.-Y. Chen, J. Peng, J. Wang and S. Peng, *Adv. Mater.*, 2023, **35**, 2305939.
11. J. Wang, H. Yang, F. Li, L. Li, J. Wu, S. Liu, T. Cheng, Y. Xu, Q. Shao and X. Huang, *Sci. Adv.*, **8**, eabl9271.
12. X. Wang, X. Wan, X. Qin, C. Chen, X. Qian, Y. Guo, Q. Xu, W.-B. Cai, H. Yang and K. Jiang, *ACS Catal.*, 2022, **12**, 9437-9445.
13. Y. Wu, R. Yao, Q. Zhao, J. Li and G. Liu, *Chem. Eng. J.*, 2022, **439**, 135699.
14. L. Wu, Q. Liang, J. Zhao, J. Zhu, H. Jia, W. Zhang, P. Cai and W. Luo, *Chin. J. Catal.*, 2023, **55**, 182-190.
15. L. Wu, W. Huang, D. Li, H. Jia, B. Zhao, J. Zhu, H. Zhou and W. Luo, *Angew. Chem., Int. Ed.*, 2024, **e202413334**.
16. X. Wang, Z. Li, H. Jang, C. Chen, S. Liu, L. Wang, M. G. Kim, J. Cho, Q. Qin and X. Liu, *Adv. Energy Mater. 2025, **15**, 2403388*.
17. H. Jin, X. Liu, P. An, C. Tang, H. Yu, Q. Zhang, H.-J. Peng, L. Gu, Y. Zheng, T. Song, K. Davey, U. Paik, J. Dong and S.-Z. Qiao, *Nat. Commun.*, 2023, **14**, 354.

18. G. Zhou, P. Wang, B. Hu, X. Shen, C. Liu, W. Tao, P. Huang and L. Liu, *Nat. Commun.*, 2022, **13**, 4106.

19. W. Gou, S. Zhang, Y. Wang, X. Tan, L. Liao, Z. Qi, M. Xie, Y. Ma, Y. Su and Y. Qu, *Energy Environ. Sci.*, 2024, **17**, 6755-6765.

20. C.-H. Li, C.-Z. Yuan, X. Huang, H. Zhao, F. Wu, L. Xin, X. Zhang, S. Ye and Y. Chen, *eScience*, 2024, 100307.

21. Y. Xu, Z. Mao, J. Zhang, J. Ji, Y. Zou, M. Dong, B. Fu, M. Hu, K. Zhang, Z. Chen, S. Chen, H. Yin, P. Liu and H. Zhao, *Angew. Chem., Int. Ed.*, 2024, **63**, e202316029.

22. S. Hao, M. Liu, J. Pan, X. Liu, X. Tan, N. Xu, Y. He, L. Lei and X. Zhang, *Nat. Commun.*, 2020, **11**, 5368.

23. H. Liu, Z. Zhang, J. Fang, M. Li, M. G. Sendeku, X. Wang, H. Wu, Y. Li, J. Ge, Z. Zhuang, D. Zhou, Y. Kuang and X. Sun, *Joule*, 2023, **7**, 558-573.

24. Y. Xue, J. Zhao, L. Huang, Y.-R. Lu, A. Malek, G. Gao, Z. Zhuang, D. Wang, C. T. Yavuz and X. Lu, *Nat. Commun.*, 2023, **14**, 8093.

25. L. Deng, S.-F. Hung, S. Liu, S. Zhao, Z.-Y. Lin, C. Zhang, Y. Zhang, A.-Y. Wang, H.-Y. Chen, J. Peng, R. Ma, L. Jiao, F. Hu, L. Li and S. Peng, *J. Am. Chem. Soc.*, 2024, **146**, 23146-23157.

26. J. Abed, J. Heras-Domingo, R. Y. Sanspeur, M. Luo, W. Alnoush, D. M. Meira, H. Wang, J. Wang, J. Zhou, D. Zhou, K. Fatih, J. R. Kitchin, D. Higgins, Z. W. Ulissi and E. H. Sargent, *J. Am. Chem. Soc.*, 2024, **146**, 15740-15750.

27. L. Li, G. Zhang, C. Zhou, F. Lv, Y. Tan, Y. Han, H. Luo, D. Wang, Y. Liu, C. Shang, L. Zeng, Q. Huang, R. Zeng, N. Ye, M. Luo and S. Guo, *Nat. Commun.*, 2024, **15**, 4974.

28. Q. Ji, B. Tang, X. Zhang, C. Wang, H. Tan, J. Zhao, R. Liu, M. Sun, H. Liu, C. Jiang, J. Zeng, X. Cai and W. Yan, *Nat. Commun.*, 2024, **15**, 8089.

29. Z. Yang, Y. Ding, W. Chen, S. Luo, D. Cao, X. Long, L. Xie, X. Zhou, X. Cai, K. Liu, X.-Z. Fu and J.-L. Luo, *Adv. Mater.*, 2025, **37**, 2417777.

30. W. Zhu, X. Song, F. Liao, H. Huang, Q. Shao, K. Feng, Y. Zhou, M. Ma, J. Wu, H. Yang, H. Yang, M. Wang, J. Shi, J. Zhong, T. Cheng, M. Shao, Y. Liu and Z. Kang, *Nat. Commun.*, 2023, **14**, 5365.

31. Y. Liu, Y. Wang, H. Li, M. G. Kim, Z. Duan, K. Talat, J. Y. Lee, M. Wu and H. Lee, *Nat. Commun.*, 2025, **16**, 1717.

32. X.-Y. Zhang, H. Yin, C.-C. Dang, H. Nie, Z.-X. Huang, S.-H. Zheng, M. Du, Z.-Y. Gu, J.-M. Cao and X.-L. Wu, *Angew. Chem., Int. Ed.*, 2025, e202425569.